Modeling single-phase transverse flows in a PWR rod bundle at low Reynolds number

Qinjun Fu, Andre Bergeron, Philippe Fillion, Yohan Davit, Michel Quintard

Modeling single-phase transverse flows in a PWR rod bundle at low Reynolds number

Qinjun Fu[a,b], André Bergeron[a], Philippe Fillion[a,*], Yohan Davit[b], Michel Quintard[b]

[a] *Université Paris-Saclay, CEA, Service de Thermo-hydraulique et de Mécanique des Fluides, 91191, Gif-sur-Yvette, France*
[b] *Institut de Mécanique des Fluides (IMFT), CNRS & Université de Toulouse, Toulouse, France*

Abstract

In normal functioning conditions, the primary component of the flow within the rod bundle of a PWR core is in the axial direction, along the rods. However, in accidental situations, such as the refilling or reflooding phase during a Loss of Coolant Accident, or a Steam Line Break accident, transverse flows may significantly affect thermal-hydraulic properties in the core. Such effects have received little attention in system codes such as CATHARE, particularly in anisotropic rod structures at low Reynolds numbers. Here, we develop macroscopic pressure drop models for flows spanning from the creeping regime to unsteady vortex shedding. The averaged model is a generalized Darcy-Forchheimer equation with an apparent permeability including a rotation matrix and a non-linear dimensionless coefficient. The constitutive relations for the intrinsic permeability matrix are derived from polynomial regressions based on results obtained from microscale numerical simulations at different flow directions and Reynolds numbers. We finally test our approach in a case where transverse flow is imposed through a differential of inlet velocities and validate by comparing results from CATHARE with those obtained from a finite element toolbox.

Keywords: Porous media approach, Effective permeability, Inertia effects, Upscaling, CATHARE

*Corresponding author
Email address: philippe.fillion@cea.fr (Philippe Fillion)

Postprint Nuclear Engineering and Design

1. Introduction

During the reflooding phase of a Large Break Loss of Coolant Accident (LBLOCA) or during the core uncovering of a Small Break LOCA (SBLOCA) or Intermediate Break LOCA (IBLOCA) in a Pressurized Water Reactor (PWR), transverse flows can develop in the core and significantly modify the cooling capabilities and peak clad temperature (Bestion and Fillion, 2019). In the dry zone, gravity and density differences induce transverse flows, which may improve (chimney effect) or degrade (divergent effect) the cooling of the hot assembly, depending on the balance between buoyancy and friction forces. While divergent crossflows from hot to cold assemblies may occur during the reflooding phase of a LBLOCA at low pressure, the chimney effect can manifest at high pressure and for relatively low velocities in SBLOCAs and IBLOCAs (Bestion et al., 2017). It may also occur during a low flow rate Main Steam Line Break (MSLB), when the dissymmetry of the temperature profile at the inlet of the core, coupled to the heterogeneity of the power distribution, leads to transverse flows from the low power to the high power region (Sung et al., 2015). The revisit by Bestion and Fillion (2019) of the process identification and ranking table (PIRT) in these situations was focused on the 3D processes in the core. The analysis showed that at low velocity with radial power differences in core, the radial pressure losses are one of the dominant phenomena with respect to cooling capabilities.

Subchannel or system thermal-hydraulic codes with 3D capabilities often attempt to capture the anisotropic properties of the rod bundle and the impact of transverse flows. In the 3D module of the system code CATHARE 3 (Préa et al., 2020), the pressure drop in the transverse direction is modeled either as described in Idel'Cik (1969) established from experiments in different arrays of cylindrical tubes or derived from the experiment EOLE (Peybernes, 2005) in a 8×8 PWR-type rod bundle. However, these relations primarily apply to turbulent flows and not to configurations at lower Reynolds numbers for transverse flows. Pressure drop data and constitutive relations in the literature only cover a limited range of geometrical configurations in term of pitch-to-diameter ratio, Reynolds numbers and flow inclinations. Inclination effects, as will be discussed later in this paper, cannot in principle be treated by assuming that the bundle axis and perpendicular directions are the principal axes. In fact, for inclined laminar flows through a PWR rod bundle, few conclusions in the literature can be directly used for modeling. For a purely transverse flow, constitutive relations for the friction coefficient are usually

taken as inversely proportional to the Reynolds number (Cumo et al., 1980) with parameters that depend on the geometry of the rod bundle. Measurements of the friction pressure drop made in Dowlati et al. (1990) across a horizontal rod bundle, with a pitch-to-diameter ratio (p/d) of 1.3, have only been performed for a limited series of Reynolds numbers. From experimental data, Zukauskas and Ulinskas (1983) proposed empirical correlations in pure transverse flow from experimental data for square arrays with different p/d ratios in the laminar and turbulent regimes. Butterworth (1979) studied the impact of the rotation angle of the flow in the transverse direction in square arrays of tubes, but only for two configurations (in-line square, and rotated square of 45°). In a square tube bundle of $p/d = 1.5$, Ebeling-Koning et al. (1986) investigated the impact of the inclination of the rod bundle on the resistance tensor, but limited in the laminar regime to data for angles of 30° and 45° with respect to the parallel axis of the tubes.

When considering the single-phase flow of a Newtonian fluid through a generic porous medium, different regimes can usually be defined based on the Reynolds number, Re (see a review in Davit and Quintard (2019)). In the case of rod bundles, transverse flows are prone to supercritical instabilities and would be very close to the behavior of a generic porous medium. $Re \sim 0$ corresponds to the creeping regime, yielding Darcy's law at the macro-scale with a linear relation between the macro-scale pressure gradient and the superficial velocity. At moderate Re numbers, the flow remains steady but inertial effects start to play a role. At the macro-scale, Darcy's law can be modified with a non-linear apparent permeability that takes into account these effects. Increasing Re yields a transition to unsteady flow at pore-scale, while averaged values may still be approximated as steady and described using Darcy's law with a non-linear apparent permeability. Finally, increasing further Re produces turbulent flows at pore-scale. Two types of macro-scale models have been proposed in this regime, depending on whether the turbulence properties can be considered quasi-periodic, which leads to another form of time-averaged non-linear Darcy's law, or features large structures that qualify as macro-scale turbulence (Jin et al., 2015), leading to macro-scale turbulent models (De Lemos, 2012).

In many models, the drag in inertial Darcy's laws is quadratic with the velocity (Forchheimer, 1901; Ergun, 1952). This correction is in fact not entirely satisfactory at all Reynolds numbers during the transition from the Darcian regime to the fully turbulent flow. At least three different flow regimes have been identified (Lasseux et al., 2011; Pasquier et al., 2017): (i) a weak in-

ertia regime that appears after the Darcian regime when nonlinear effects start being non-negligible and a cubic correction can be used, (ii) a strong inertia regime where the growth of the correction term is slowing down and is approximately quadratic in Re, i.e., a Forchheimer type of correction, (iii) possibly unsteady macro-scale turbulent flow requiring a macro-scale turbulence model (De Lemos, 2012). It is important to emphasize that transitions in regimes are not very sharp, so that Re^n scalings remain only modellng approximations. The case of flows along the bundle axis, which involves subcritical instabilities with a specific transition to turbulence, is not considered in this paper, i.e., no-correction will be made to the linear regime.

In this paper, our goal is to propose a 3D friction model that is valid at low Reynolds numbers for transverse flows, therefore limiting ourself to steady-state solutions at the macro-scale. To this end, we use a porous media approach to derive a *generalized* Darcy-Forchheimer equation with an apparent permeability matrix that takes into account inertial effects and the anisotropy of the porous medium. The constitutive relation for the permeability is obtained by performing microscale numerical simulations within a periodic Unit Cell (UC), in our case a subchannel surrounded by four rods. The apparent permeability is decomposed into an intrinsic permeability matrix, a rotation matrix representing a change in the average flow direction and a dimensionless coefficient. The intrinsic permeability matrix is calculated from simulation results of a creeping flow along principle axes (x, y and z axes). The two other variables take the form of polynomial interpolations obtained through a series of calculations with flow at various Reynolds numbers and average directions. From the apparent permeability, wall friction coefficients are derived and introduced in the CATHARE code as a *new model*. This model is tested against numerical cases reproducing asymmetric velocities at the inlet of two adjacent rod bundles, generating transverse flows. We also compare and validate our results against a finite-element implementation of the generalized Darcy-Forchheimer approach using the FEniCS toolbox (Alnæs et al., 2015).

2. Models and methods

2.1. Microscale flow problem, geometry and direct numerical simulations in TrioCFD

We consider the following incompressible Navier-Stokes equations (solid σ and fluid β)

$$\nabla \cdot \mathbf{u} = 0 \text{ in the fluid domain } \mathcal{V}, \tag{1}$$

$$\rho \left(\frac{\partial \mathbf{u}}{\partial t} + \mathbf{u} \cdot \nabla \mathbf{u} \right) = -\nabla p + \rho \mathbf{g} + \mu \nabla^2 \mathbf{u} \quad \text{in } \mathcal{V}, \tag{2}$$

with a no-slip/no-penetration condition

$$\mathbf{u} = 0 \text{ on the fluid-solid boundary } A_{\beta\sigma}, \tag{3}$$

with p a pore-scale pressure field, $\mathbf{u}$ the velocity, ρ the volumetric mass, μ the dynamic viscosity and $\mathbf{g}$ the gravity acceleration

In the framework of a multi-scale analysis through the volume averaging technique, see Sec. 2.2, we will introduce Darcy-scale governing equations for the average or filtration velocity, $\mathbf{V}_f$, and the intrinsic average pressure, P, defined as:

$$\mathbf{V}_f = \frac{1}{|\mathcal{V}|} \int_{\mathcal{V}_\beta} \mathbf{u} \, d\mathcal{V}, \; P = \frac{1}{|\mathcal{V}|} \int_{\mathcal{V}_\beta} p \, d\mathcal{V}, \tag{4}$$

where $\mathcal{V}$ is some averaging volume and $\mathcal{V}_\beta$ is the volume occupied by the fluid within $\mathcal{V}$.

In order to calculate effective properties in the Darcy-scale model, we will solve a slightly modified version of the initial Navier-Stokes problem. The Navier-Stokes equations are written in terms of a pressure deviation, $\tilde{p} = P - p$ and a source term $\mathbf{F} = \nabla P - \rho \mathbf{g}$. We have

$$\rho \left(\frac{\partial \mathbf{u}}{\partial t} + \mathbf{u} \cdot \nabla \mathbf{u} \right) = -\nabla \tilde{p} - \mathbf{F} + \mu \nabla^2 \mathbf{u} \quad \text{in } \mathcal{V}. \tag{5}$$

This problem will be used later to calculate the apparent permeability in the macro-scale equations by resolving the above problem over a periodic unit cell representative of the structure. In this latter case, it is convenient to impose the following periodic boundary conditions

$$\mathbf{u}(\mathbf{x} + \mathbf{l}_i, t) = \mathbf{u}(\mathbf{x}, t) \; ; \; \tilde{p}(\mathbf{x} + \mathbf{l}_i, t) = \tilde{p}(\mathbf{x}, t) \quad i = 1, 2, 3 \tag{6}$$

where $\mathbf{l}_i$ stands for the periodic medium lattice vectors, along with initial condition

$$\mathbf{u}(\mathbf{x}, t = 0) = \mathbf{u}_0(\mathbf{x}) \text{ and } \tilde{p}(\mathbf{x}, t = 0) = \tilde{p}_0(\mathbf{x}), \tag{7}$$

and the uniqueness condition for the pressure deviation

$$\int_{\mathcal{V}_\beta} \tilde{p}\, d\mathcal{V} = 0. \tag{8}$$

With this set of boundary and initial conditions, flow only occurs in response to the volumetric force $\mathbf{F}$. We finally introduce a Reynolds number as

$$Re_{D_h} = \frac{\rho ||\mathbf{V}_f|| D_h}{\epsilon \mu}, \tag{9}$$

with the hydraulic diameter $D_h = \frac{4|\mathcal{V}_\beta|}{|A_{\beta\sigma}|}$ and the porosity

$$\epsilon = \frac{1}{|\mathcal{V}|} \int_{\mathcal{V}_\beta} d\mathcal{V} = \frac{|\mathcal{V}|}{|\mathcal{V}_\beta|}. \tag{10}$$

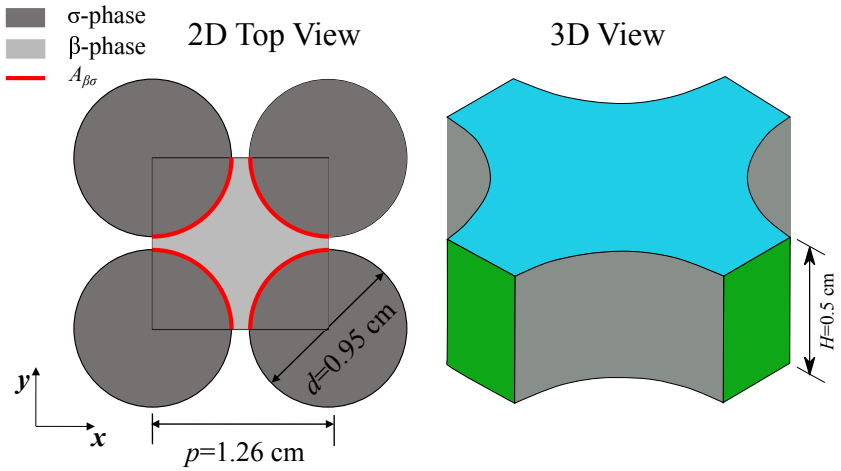

Figure 1: Unit-cell of the rod bundle.

Pore-scale simulations are performed using the code TrioCFD (Angeli et al., 2015), which solves a wide range of flow problems including turbulent, mono or multi-phase flows and fluid/solid couplings. The spatial

discretization in TrioCFD is achieved by means of hybrid finite-volume element method, where the velocity is evaluated at the center of the faces of tetrahedral elements and the pressure at both the center and vertices of the element. A 1st order Euler backward implicit scheme is used for time integration. The discretized momentum balance equations are solved using SOLA pressure projection method (Bieder et al., 2014; Angeli et al., 2015; Bieder et al., 2018). The Poisson equation is solved by a Cholesky method. The solver convergence threshold was set to be 10^{-8}. The stationary threshold was 10^{-11}.

The geometries used for our study are presented in Fig 1. Following a numerical convergence study, meshes consisting of about 360,000 tetrahedral elements for one unit-cell are generated using SALOME (SALOME, 2023). In order to analyse the impact related to the mesh density, an averaged velocity sensibility between two meshes has been conducted both in the two cases of transverse flow and flow for an applied force inclined at an angle of 5°, and for Reynolds number ranging between 1 and 535. The coarsest and finest meshes were respectively of 360,000 and 3.3 million cells, therefore with a density ratio of 10 between the two. For very low Reynolds numbers, the averaged velocity sensitivity regarding the meshing density is negligible. The sensibility to the meshing density rises with the Reynolds number, the effect being more significant for the averaged velocity than for the flow inclination. In case of transverse flow the largest averaged velocity discrepancy between the two meshes is about 4.3% for a Reynolds number of 535 leading to a discrepancy of 2% on the f coefficient introduced in equation (12), which does not really affect macroscopic calculations at the porous scale. In case of an inclined flow, the largest discrepancy on the resulting angle is about 0.2°. It has also been observed in the transverse flow configuration for the Reynolds number of 535 that doubling the mesh density (7.2 million of cells) of the finest mesh has a quite negligible influence on results. As the CPU hours requested by the finest mesh for one calculation is ten times more than that for the coarsest mesh and due to the large number of computations needed for the elaboration of the friction correlation it has been decided to keep the coarsest mesh of 360,000 cells for our calculations.

The unsteady flow within a subchannel may have 3D structures and the height of the computation domain should be large enough to correctly predict the flow field. Since our final goal is to calculate effective permeabilities, we checked that the average velocity was the same for $H = 1$ cm and $H = 0.5$ cm

in the case of a transverse flow at $Re_{D_h} = 684$[1] inclined at about 5° to z-axis, i.e., a generic case at a high value of the Re number in the chosen range.

In the x and y directions, it is also important for the accuracy of the macro-scale model to have enough unit-cells. In the creeping flow regime, a single unit-cell is enough since the Stokes solution is truly periodic. In recent studies, it has been suggested that few unit-cells are sufficient since the porous medium filters out the largest length-scales of the coherent structures in inertial flows (Hosseini et al., 2012; Soulaine and Quintard, 2014; Jin et al., 2015). However, the link between the number of UCs and precision/stability is not trivial. In Agnaou et al. (2016), for instance, it was found that the critical Reynolds number of the first Hopf bifurcation depends on the number of UCs in the domain, in particular for ordered structures.

To gain further insight into this issue, we solved the flow problem corresponding to a volumetric force along the x-direction for the domain with one UC (Figure 1) and for a domain composed of three UCs in the x-direction. The velocity is averaged over the whole domain for the reference UC and within the central unit cell for the domain consisting of 3×1 UCs. For calculations at $Re_{D_h} \simeq 320$ and $Re_{D_h} \simeq 684$, a similar flow pattern was predicted in both cases and the difference of averaged transverse velocity was only about 2%, allowing us to consider only one UC for the remainder of this work.

2.2. Method for calculating effective parameters from microscale results

While there are various ways of writing the macro-scale equation in the steady-state case, we adopt the form involving an apparent permeability (Pauthenet et al., 2018)

$$\mathbf{V}_f = -\frac{\mathbf{K}_{app}}{\mu} \cdot (\nabla P - \rho \mathbf{g}) = -\frac{\mathbf{K}_{app}}{\mu} \cdot \mathbf{F}, \tag{11}$$

with the Darcy velocity and intrinsic pressure already defined in Sec. 2.1. $\mathbf{K}_{app}$ is a non-linear apparent permeability that we further decompose as

$$\mathbf{K}_{app} = \frac{\mathbf{R} \cdot \mathbf{K}_{int}}{1 + f}, \tag{12}$$

[1]Calculations follow the following scheme: the volumetric force is imposed which in turn generates the velocity field, hence any value of Re.

where $\mathbf{R}$ is a rotation matrix, $\mathbf{K}_{int}$ is the intrinsic permeability matrix, and f is a dimensionless coefficient that depends on the flow conditions. For a creeping flow ($Re_{D_h} \ll 1$), $\mathbf{R} = \mathbf{I}$ and $f = 0$, thus $\mathbf{K}_{app} = \mathbf{K}_{int}$. For a flow with $Re_{D_h} \gtrsim 1$, inertial effect will yield different values of $\mathbf{R}$ and f.

The idea is now to estimate each of these, $\mathbf{R}$, $\mathbf{K}_{int}$ and f, separately. To calculate the intrinsic permeability, we can simply solve the modified flow problem over a periodic system for $Re_{D_h} \simeq 0$, and determine the diagonal components by imposing successively the volumetric force, $\mathbf{F}$, along the x, y and z directions. We obtain the following anisotropic tensor

$$\mathbf{K}_{int} \simeq \begin{bmatrix} 4.94 \times 10^{-7} & 0 & 0 \\ 0 & 4.94 \times 10^{-7} & 0 \\ 0 & 0 & 1.54 \times 10^{-6} \end{bmatrix} \mathrm{m}^2. \tag{13}$$

Discussion concerning the comparison of the obtained permeability values is given in Section 3.3.

By using the properties of a rotation matrix, we can further calculate f and $\mathbf{R}$ as follows

1. Since the rotation matrix does not change the norm of the rotated vector, f can hence be calculated as

$$f = \begin{cases} \dfrac{\parallel \mathbf{K}_{int} \cdot \mathbf{F} \parallel}{\parallel \mathbf{V}_f \parallel \mu} - 1, \text{ if } \parallel \mathbf{V}_f \parallel > 0; \\ 0, \text{ if } \parallel \mathbf{V}_f \parallel = 0. \end{cases} \tag{14}$$

2. In order to calculate the rotation matrix $\mathbf{R}$ with given $\mathbf{K}_{int}$, $\mathbf{V}_f$ and $\mathbf{F}$, the effect of rotation matrix can be seen as rotating a unit vector $\mathbf{e}_{int} = \frac{\mathbf{K}_{int} \cdot \mathbf{F}}{\|\mathbf{K}_{int} \cdot \mathbf{F}\|}$ to a unit vector $\mathbf{e}_u = \frac{\mathbf{V}_f}{\|\mathbf{V}_f\|}$,

$$\mathbf{e}_u = \mathbf{R} \cdot \mathbf{e}_{int}. \tag{15}$$

In application of our study, a vector in 3D space, such as $\mathbf{F}$ or $\mathbf{V}_f$, is defined by three independent variables: the angle between the vector and the z-axis, the angle between the projection on x-y plane of this vector and the x-axis, and the norm of this vector. We write that as α_F, θ_F and $\parallel \mathbf{F} \parallel$ or α, θ and $\parallel \mathbf{V}_f \parallel$ with an example for $\mathbf{F}$ shown in Figure 2a.

A full 3D study of the apparent permeability of a PWR type rod bundle requires calculations covering $0° \leq \alpha_F \leq 90°$, $0° \leq \theta_F \leq 45°$ and a series of value of $\parallel \mathbf{F} \parallel$ corresponding to a certain range of the Reynolds number after

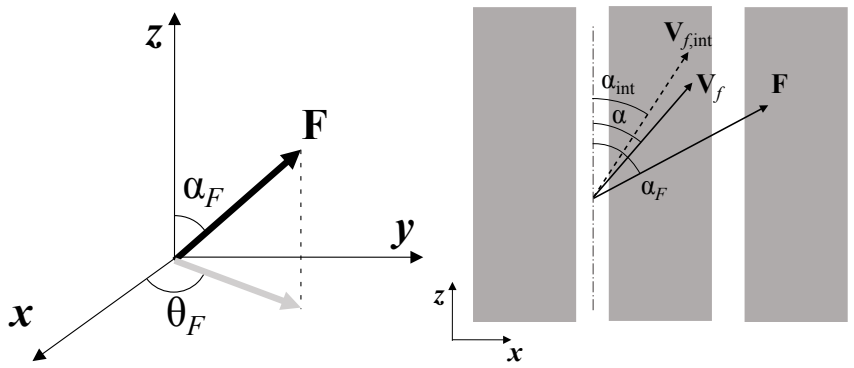

(a) (b)

Figure 2: Definition of angles in the rod bundle. (a) α_F and θ_F define the macroscopic pressure gradient orientation. (b) Case with $\theta_F = 0$. $\mathbf{V}_{f,int} = -\mathbf{K}_{int} \cdot \mathbf{F}/\mu$ denotes the velocity calculated directly with the intrinsic permeability without considering inertia effect (i.e., $f = 0$ and $\mathbf{R} = \mathbf{I}$). Its inclination to the z-axis is α_{int}. The angle between the final velocity $\mathbf{V}_f$ and the z-axis is represented by α. For a flow in the Darcy regime, $\mathbf{V}_{f,int}$ and $\mathbf{V}_f$ are equal. The differences of orientation and magnitude of $\mathbf{V}_{f,int}$ and $\mathbf{V}_f$ are related to $\mathbf{R}$ and f, respectively.

taking into account the symmetry properties of such geometry. In this paper, we concentrate on the impact of the inclination with respect to the z-axis. Cases where the flow can be inclined within the $x-y$ plane will be considered at a later stage. Therefore, the current study concerns flow parallel to x-z plane i.e., $\theta_F = 0°$ and $\theta = 0°$. With this hypothesis and writing the rotated angle in matrix $\mathbf{R}$ as $\gamma_y = \alpha - \alpha_{int}$, we have

$$\mathbf{R} = \begin{bmatrix} \cos(\gamma_y) & 0 & \sin(\gamma_y) \\ 0 & 1 & 0 \\ -\sin(\gamma_y) & 0 & \cos(\gamma_y) \end{bmatrix}. \tag{16}$$

2.3. Macroscale Darcy-Forchheimer model and finite-element resolution in FEniCS

Once $\mathbf{R}$ and f have been tabulated, Darcy-scale equations may be solved in an independent manner. The fluid is considered incompressible and flow is governed by

$$\nabla \cdot \mathbf{V}_f = 0, \tag{17a}$$

$$\mathbf{V}_f = -\frac{\mathbf{R}\cdot\mathbf{K}_{int}}{\mu\,(1+f)}\cdot(\nabla P - \rho\mathbf{g})\,. \tag{17b}$$

This system of equations is solved in the framework of the open-source finite element automation software FEniCS (Alnæs et al., 2015). The code is written in python and makes use of FEniCS Finite-Element classes. The domain is discretized with triangles. A mixed formulation is used with BDM (Brezzi-Douglas-Marini) elements of order k for velocity and DG (discontinuous element) elements of order $k-1$ for pressure. An order $k=1$ was found sufficient for accuracy needs. The default linear algebra backend in FEniCS is PETSc. Picard iteration is used during the solving process to handle non-linearities.

2.4. Macroscale modeling in CATHARE 3

In the CATHARE code, mass, momentum and energy conservation equations are time-space averaged for each phase. The time averaging process filters the pseudo-random variations of the flow variables due to turbulence and two-phase intermittence (Chandesris et al., 2013). The space averaging process takes into account the interactions between fluid and solid phases. Several phenomena are modeled and validated on specific separate effect tests. This includes the turbulent diffusion of heat and momentum and the heat and momentum dispersion due to space averaging (Bestion et al., 2018). Elements of validation at the subchannel scale for these terms have been obtained against data measured in rod bundle geometries, mostly in 5×5 or 6×6 layouts where the border effects can affect the flow, at both high and moderate Reynolds numbers, and with or without mixing grids (Valette, 2012; Chandesris et al., 2013; Alku, 2017; Fu et al., 2019). In addition to these phenomena, 3D wall friction models have to be developed and validated for core rod bundles.

Since only single-phase flow is involved in this study, the terms related to two-phase phenomena in CATHARE governing equations are removed for simplicity and clarity. Neglecting the turbulent and dispersive effects in the momentum equation, and the turbulent and dispersive heat flux in the energy equation, and considering the heat flux equal to 0 in our study, the balance equations for the time and spatially averaged fields can be written as

- Mass balance equation

$$\frac{\partial}{\partial t}(\epsilon\rho) + \nabla\cdot(\epsilon\rho\mathbf{V}) = 0, \tag{18}$$

- momentum balance equation

$$\rho\left[\frac{\partial}{\partial t}\mathbf{V}+\mathbf{V}\cdot\nabla\mathbf{V}\right]+\nabla P=\boldsymbol{\tau}_w+\boldsymbol{\tau}_s+\rho\mathbf{g} \tag{19}$$

- energy balance equation

$$\frac{\partial}{\partial t}\left(\epsilon\rho e\right)+\nabla\cdot\left(\epsilon\rho e\mathbf{V}\right)+P\left[\frac{\partial\epsilon}{\partial t}+\nabla\cdot\left(\epsilon\mathbf{V}\right)\right]=0. \tag{20}$$

In the above equations, $\rho, \mathbf{V}(\epsilon\mathbf{V}=\mathbf{V}_f), e, P$ are temporal and spatial intrinsic averaged density, velocity, internal energy and pressure of the considered (vapour or liquid) phase, ϵ is the porosity and $\mathbf{g}$ is the gravity acceleration.

The pressure drop in CATHARE is thought of as being caused by two different types of frictions: the singular friction $\boldsymbol{\tau}_s$ and the regular (or wall) friction $\boldsymbol{\tau}_w$. The singular friction captures the effect of the singularies such as sudden flow surface restriction or expansion (Rehme, 1973). In the rod axis direction, it is generated by the spacers. The regular friction term appearing in equation (19) is modeled as:

$$\boldsymbol{\tau}_w=-\frac{2\rho}{D_h}\mathbf{C}_f^{\mathrm{F}}\cdot\mathbf{V}||\mathbf{V}||=-\frac{2}{D_h}\rho\begin{pmatrix}C_{f_x}^F & & \\ & C_{f_y}^F & \\ & & C_{f_z}^F\end{pmatrix}\cdot\mathbf{V}||\mathbf{V}||. \tag{21}$$

For 3D simulations in rod bundles, the single-phase friction factors $C_{fi,i=x,y,z}^F$ are simply extrapolated from correlations obtained in tubes. Thus, the Fanning friction factor $C_{f_z}^F$ in the axial direction z ($C_{f_z}^F=\frac{1}{4}C_{f_z}$, where C_{f_z} is the Darcy coefficient) is calculated considering the maximum coefficient in laminar and turbulent regimes (Blasius law and high Reynolds number regime, corresponding to the limit of the Colebrook equation with a relative rugosity of 10^{-4}), as

$$C_{f_z}^F=\frac{1}{4}C_{f_z}=\max\left(\frac{16}{\mathrm{Re}_{D_h}};\frac{0.079}{\mathrm{Re}_{D_h}^{0.25}};0.003\right), \tag{22}$$

where Re_{D_h} is the previously defined Reynolds number depending on the hydraulic diameter, this time calculated as

$$\mathrm{Re}_{D_h}=\frac{\rho||\mathbf{V}||D_h}{\mu}. \tag{23}$$

The corresponding transition Reynolds numbers are $\mathrm{Re}_{D_h} = 1169$ for the transition from laminar to the turbulent regime, and $\mathrm{Re}_{D_h} = 480845$ for the transition to the high Reynolds turbulent regime. In the standard 3D modellng, expression (22) is also used in the x- and y-directions, and thus the friction coefficient is isotropic.

To model the total friction pressure drop in the transverse direction, an anisotropic correlation is used in CATHARE for 3D simulations. The corresponding pressure drop coefficient is usually deduced from Idel'Cik (1969) or EOLE (Peybernes, 2005). In Idel'Cik (1969), an experimental correlation in an array of tubes depending on the pitch p and the diameter d is given for Reynolds numbers Re_d (determined with tube diameter and velocity at the narrow gap between two tubes) from 3×10^3 to 10^5 and for inclinations of the flow with respect to the rod axis from 30° to 90° (pure transverse flow). In Peybernes (2005), experiments were carried out in a test section called EOLE, including a 8×8 rod bundle similar to those of PWR fuel rod bundle ($p = 1.26$ cm, $d = 0.95$ cm), with Reynolds numbers Re_d from 7×10^3 to 3.7×10^4 and inclination from 30° to 90°. Expressions in Idel'Cik (1969) and Peybernes (2005) for the pressure drop coefficient per rod row are written as a function of the inclination angle to the pressure drop coefficient in a pure transverse flow. It is to be noted that the starting point for the development of the correlations is the case of axis-flow, with a physics completely different from the transverse flow at low Reynolds numbers, as discussed in the introduction. In particular, these correlations are limited to turbulent flows and are thus not suitable for laminar and transition regimes. We list below the potential discrepancies that can be generated by this choice:

- Flow transitions may occur at different Reynolds numbers with respect to the pure transverse case,
- General anisotropic effects cannot be represented by Eq. 21,
- Eq. 21 has the form of a classical Forchheimer term and does not capture the various stages described in the Introduction.

3. New constitutive models for pressure drops through rod bundles

As presented in Section 2.2, the apparent permeability reads

$$\mathbf{K}_{app} = \frac{\mathbf{R} \cdot \mathbf{K}_{int}}{1 + f}.$$

Here, our goal is to derive constitutive models for f and $\mathbf{R}$ from direct numerical simulations with TrioCFD of the problem described in Sec. 2.1.

3.1. Constitutive relations for transverse flow

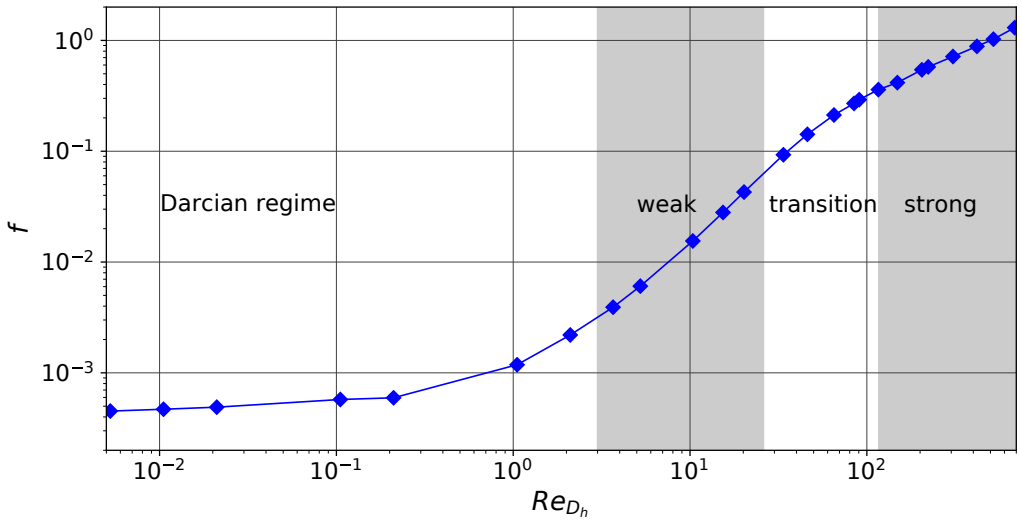

Figure 3: Evolution of f with Re_{D_h} in a pure transverse flow ($\alpha = 90°$) and identification of the flow regimes.

Figure 3 shows the results of TrioCFD simulations for the evolution of f as a function of Re_{D_h}. The Darcian regime is recovered at very low Reynolds numbers ($\mathrm{Re}_{D_h} \lesssim 10^{-1}$), where f is nearly invariant and close to zero. As expected for Stokes flow, streamlines are symmetric about both horizontal (x-y) and vertical (y-z) planes passing through the subchannel center (Figure 4a). A pair of counter-rotating vortices are also generated in the throat zone between two adjacent rods along the x-direction.

Consistent with the literature (Rojas and Koplik, 1998; Skjetne and Auriault, 1999; Lasseux et al., 2011; Pasquier et al., 2017), different regimes can be identified beyond the linear Darcy flow, as shown in Figure 3. These regimes are (a) a weak inertia regime ($4 \leq \mathrm{Re}_{D_h} \leq 20$). Figure 4b shows that the flow starts losing symmetry about the vertical plane and recirculation regions between adjacent rods grow slightly. Then, we have (b) a transition regime for $34 \leq \mathrm{Re}_{D_h} \leq 116$ where the flow is no longer symmetric about the vertical plane and a pair of symmetric contra-rotating vortices starts

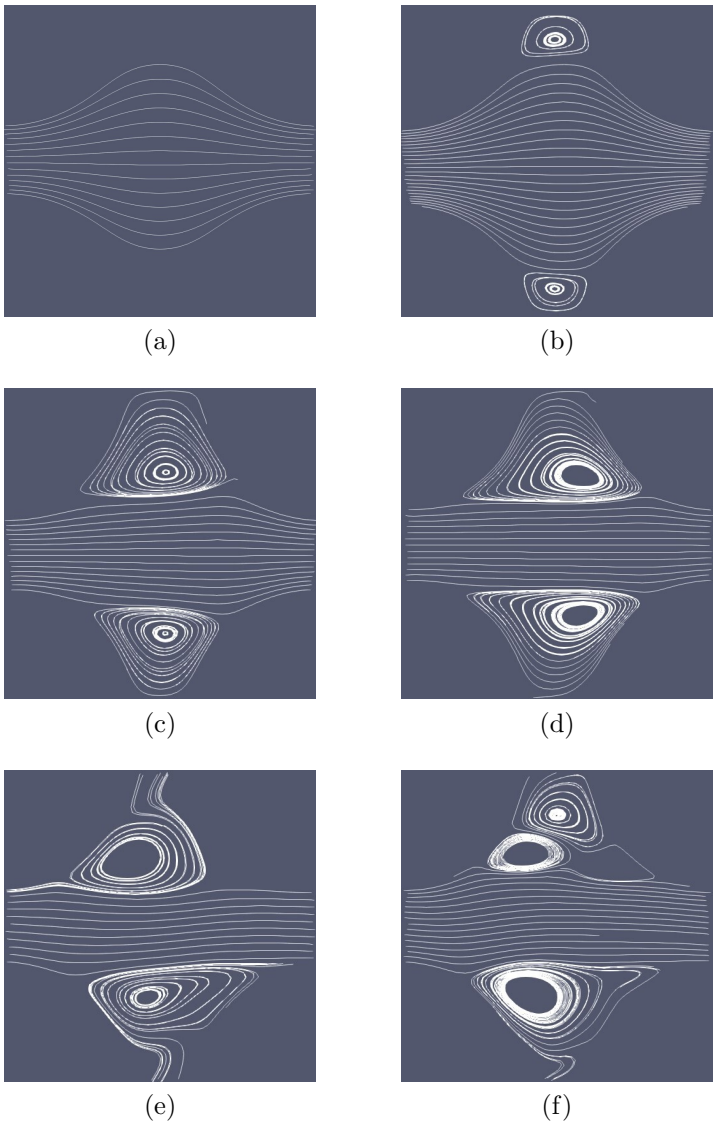

Figure 4: Pore-scale streamlines of transverse flow at different Reynolds numbers: (a) $Re_{D_h} = 1.0 \times 10^{-6}$ in the Darcian regime, (b) $Re_{D_h} = 10$ in the weak inertia regime, (c) $Re_{D_h} = 83$ in the transition regime, (d) $Re_{D_h} = 319$ in the strong inertia regime, (e)(f) $Re_{D_h} = 653$, with pore-scale unsteady flow at different times.

forming and growing until they occupy almost all the throat zone as shown in Figure 4c. Finally, we have (d) a strong inertia regime ($120 \leq \mathrm{Re}_{D_h}$) where f is approximately linear with Re_{D_h}. This regime is called quadratic in the literature since the apparent permeability depends mainly upon the square of the Reynolds number. The fluid flows primarily through the gap between two rods, with a pair of vortices shifted in the direction of the flow as shown in Figure 4d. When the Reynolds number increases, the flow becomes unsteady at pore-scale with the appearance of vortex shedding as shown in Figure 4e and 4f. Although the flow is unsteady at pore-scale, the fluctuations of macroscopic properties are negligible (the difference of magnitude of macroscopic velocity obtained at different time steps are less than 1% and the relation of macroscopic velocity and pressure gradient can be described by a Darcy's law with an apparent permeability).

If we approximate f piecewise, assuming that the weak inertia regime corresponds to f scaling as $\mathrm{Re}_{D_h}^2$ and the two other regimes to f scaling linearly with Re_{D_h}, then the least square fits for the three regimes are (see also the plot in Figure 5):

$$f_{\mathrm{tr}}\left(\mathrm{Re}_{D_h}\right) = \begin{cases} 0.00010\mathrm{Re}_{D_h}^2 + 0.0037 & \text{weak inertia,} \quad 0 < \mathrm{Re}_{D_h} \leq 25.5, \\ 0.00346\mathrm{Re}_{D_h} - 0.0194 & \text{transition,} \quad 25.5 < \mathrm{Re}_{D_h} \leq 117, \\ 0.00163\mathrm{Re}_{D_h} + 0.1948 & \text{strong inertia,} \quad 117 < \mathrm{Re}_{D_h} \leq 684. \end{cases} \tag{24}$$

where f_{tr} denotes the correlation of f in a pure transverse flow, for three considered regimes.

Of course, the exact boundary between these different regimes is not physically defined in the absence of clear bifurcation mechanisms. In fact, transitions occur where the dependence does not clearly scale with $\mathrm{Re}_{D_h}^n$. The proposed relations are simply a way of approximating these transitions, without a strong link with the underlying physics of the problem. The first branch of the correlation does not ensure that tends towards zero when $Re_{Dh} \to 0$, thus inducing a modification of the intrinsic permeability. However, this modification is very small, i.e., a factor 1.0037. It was kept for computational purposes, as it allowed to suppress an insignificant case.

3.2. Constitutive model accounting for flow inclination

Here, we investigate the dependence of f and γ_y on the flow inclination. Three series of tests, each at a constant Reynolds number ($Re_{D_h} = 90$, $Re_{D_h} = 225$, and $Re_{D_h} = 400$), are performed, with the pressure gradient

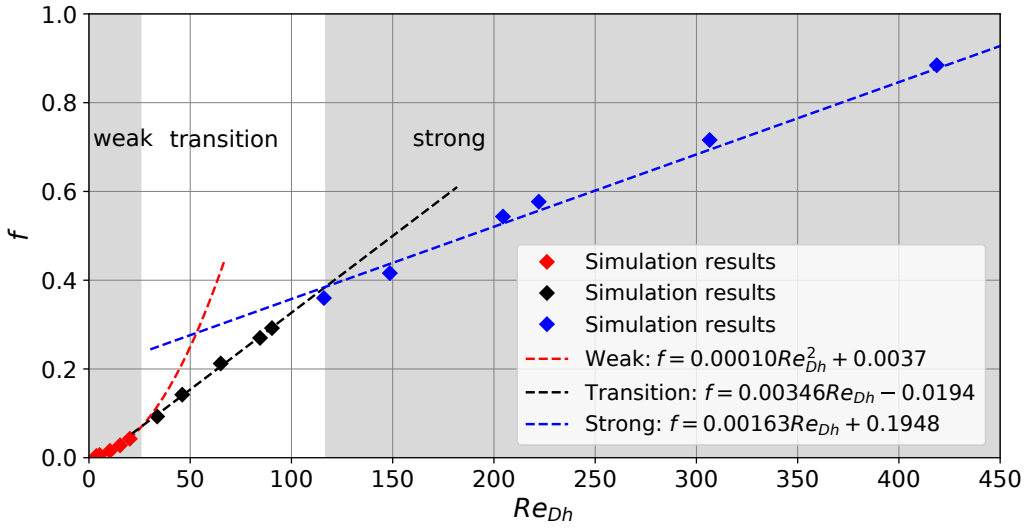

Figure 5: Correlations of f in a pure transverse flow for the weak, transition and strong regimes.

directions and consequently the velocity angles varying approximately from $0°$ (along z-axis direction) to $90°$ (along x-axis direction).

Figure 6a shows how f varies with α. For all three Reynolds numbers, f increases rapidly once the flow deviates from the axial direction. The growth rate then decreases with α and f becomes nearly stable for $\alpha \gtrsim 45°$. We also see in Figure 6b that the ratio of f over f_{tr}, which corresponds to f in the transverse direction, is nearly invariant with the Reynolds number. It is therefore convenient to describe f as a product of an angle factor Φ multiplying f_{tr}:

$$f(Re_{Dh}, \alpha) = \Phi(\alpha)\ f_{\text{tr}}(Re_{D_h}) \tag{25}$$

In this study, we propose an angle factor with the following form

$$\Phi\left(\alpha\right) = \begin{cases} \sin^{0.4}(2\alpha), & 0° \leq \alpha \leq 45°; \\ 1.0, & 45° < \alpha \leq 90°. \end{cases} \tag{26}$$

Figure 6b further shows that Φ predicted by this equation is in good agreement with simulation results, in particular for relatively large Reynolds number.

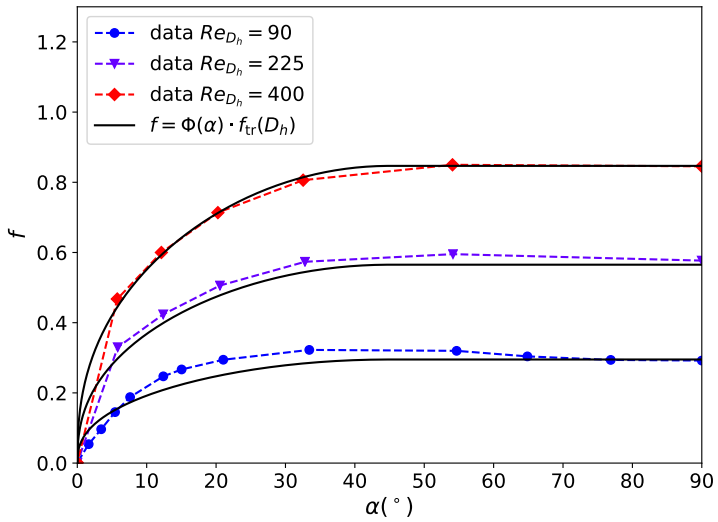

(a)

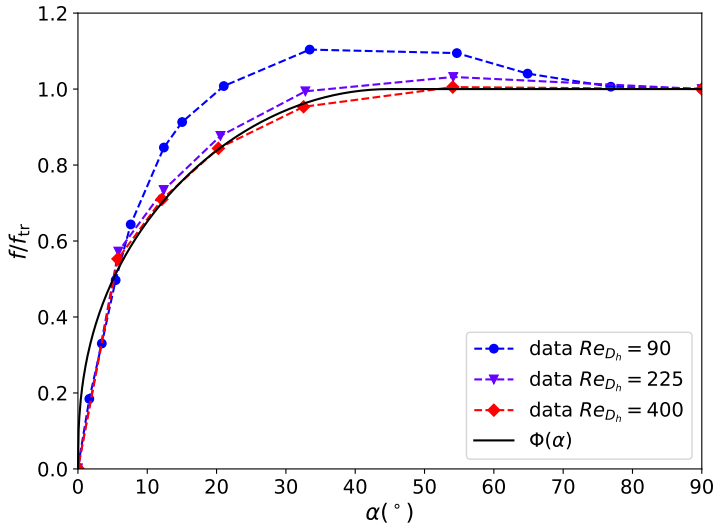

(b)

Figure 6: (a) Variation of f with α at different Reynolds numbers, (b) variation of ratio of f over f_{tr} (f at $\alpha = 0°$) with α at different Reynolds numbers, and angle functions, i.e., Eq (26).

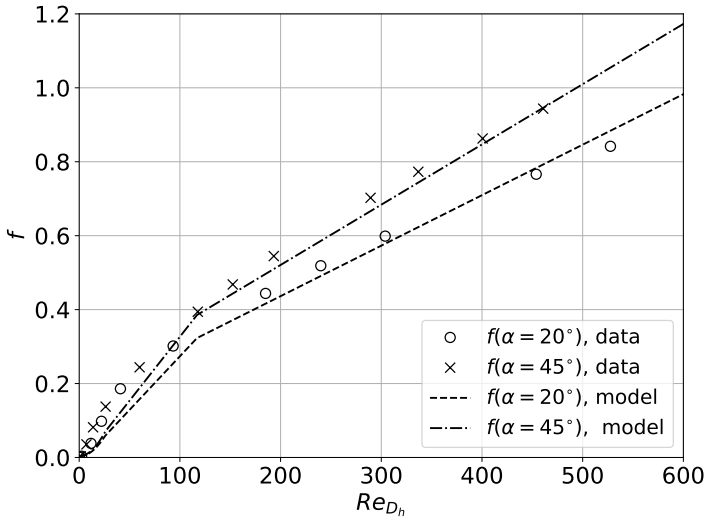

Figure 7: Comparison of the proposed model for f (equation (25) with data from simulations results with fixed inclination angles.

Comparisons of f predicted by Eqs (25) (combining Eqs (26) and (24)) against simulation results are presented in Figure 6a, showing good agreement with both Re_{D_h} ranging from 90 to 400 and α. Considering the difference between an inclined flow and a pure transverse flow, in particular regarding the onset of instabilities and the behavior of vortices, two complementary series tests with fixed inclination angle, $\alpha = 20°$ and $\alpha = 45°$, and increased Reynolds numbers were performed in order to confirm the accuracy of relations of f and γ_y. Results are plotted in Figure 7. In general, the value of f predicted by Eq (25) is in good agreement with the simulation results for $Re_{D_h} > 100$. For the lowest Reynolds numbers, however, the transitions between the different regimes identified in transverse flow are not well captured for the inclined flows, and the proposed model given by equation (25) may be improved in future work.

We now consider the rotation angle about the y-axis, γ_y, in the three series tests. Results are plotted in Figure 8a and Figure 8b. We see that dependence of γ_y upon the three different Reynolds numbers is rather weak compared to the effect of the angle, with a difference of rotated angles of less than 1° at maximum. For the remainder of this work, we therefore assume that the rotation angle depends only on the flow direction. Results further

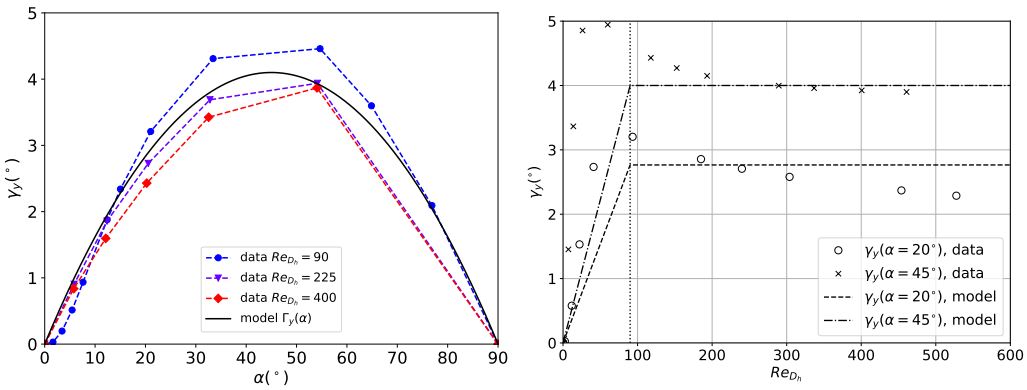

(a) (b)

Figure 8: Comparison of the proposed model of rotation angle about y-axis γ_y with (a) data from simulation results for fixed Reynolds numbers (b) data from simulation results for fixed inclination angles.

show that the maximum rotation angle $\gamma_{y,\max}$ occurs for α around 45°. To describe this, we use a parabolic relation for γ_y with constraints: a) $\gamma_y = 0°$ at $\alpha = 0°$, b) $\gamma_y = \gamma_{y,\max}$ at $\alpha = 45°$, and c) $\gamma_y = 0°$ at $\alpha = 90°$. This yields the following model function

$$\gamma_y = \Gamma_y(\alpha) = \gamma_{y,\max}\left[1 - \left(\frac{45 - \alpha}{45}\right)^2\right], \qquad 0° \leq \alpha < 90°, \tag{27}$$

where $\gamma_{y,\max} \approx 4$, which is in good agreement with the numerical calculations (see Figure 8a) for $90 \leq Re_{D_h} \leq 400$.

The value of γ_y is also presented in Figure 8b for the same complementary series tests with fixed inclination angle as in the analysis for f. Starting from zero for the Reynolds number, the rotation angle relative to the pure Darcy case increases quickly once inertial effects are involved, reaching a maximum value around Re_{D_h} equal to 80-90, then decreases and becomes nearly constant. The maximal value of γ_y is also obtained at $\alpha \simeq 45°$ with this test. Although the rotation angles at low Reynolds numbers are quite different compared to the value predicted by Eq.(27), considering that our interest for applying the apparent permeability model is with relatively high Reynolds number and that the impact of rotation matrix is negligible in the current configuration (see details in next section), we provide a rough correlation with a linear dependence upon the Reynolds number for γ_y at

low Reynolds numbers ($Re_{D_h} < 90$):

$$\gamma_y = \gamma_y(\alpha, Re_{D_h}) = \begin{cases} \Gamma_y(\alpha)\frac{Re_{D_h}}{Re_\gamma} & Re_{D_h} \leq Re_\gamma \\ \Gamma_y(\alpha) & Re_{D_h} > Re_\gamma \end{cases}, \tag{28}$$

where $Re_\gamma = 90$ and $\Gamma_y(\alpha)$ is given by equation (27).

We finally have a whole set of validated correlations for f and γ_y within the first quadrant of the x-z plane. By using the symmetry properties of the rod bundle, the constitutive model can be extended into the whole domain ($0° \leq \alpha < 360°$).

Before comparing the proposed model to macro-scale models classically used in nuclear engineering, it is important to emphasize the difference of our generalized model to Forchheimer formulations classically encountered in the porous medium literature. Classical Forchheimer formulations have a Darcy term and a quadratic term depending only on the velocity but not the velocity orientation. Analysis of various porous media structure, including the one proposed in this paper, have emphasized the following discrepancies with this classical Forchheimer model:

- many more regimes can be observed, in terms of Reynolds number, with non-quadratic dependence,
- these effects are more pronounced for relatively simple unit cells, i.e. non-disordered media, which is the case for nuclear reactor structures, In particular, the quadratic regime may appear for relatively large Reynolds number, and even be rapidly replaced by other regimes, e.g. macro-scale turbulence.
- anisotropy effects induced by the non-linearity of the problem are not taken into account. Our results, and previous results in the literature, show that this is a very rough approximation that can lead to significant errors.

3.3. Comparison of constitutive models with literature models used in nuclear engineering

The friction term $\boldsymbol{\tau_w}$ in Eq. (19) can be rewritten as

$$\boldsymbol{\tau_w} = -\mathbf{C}_f \cdot \frac{\rho \mathbf{V}_f \parallel \mathbf{V}_f \parallel}{2D_h\epsilon^2}. \tag{29}$$

thanks to the relation $\mathbf{V} = \mathbf{V}_f/\epsilon$. Combining the above equation with the generalized Darcy-Forchheimer model, i.e., Eq. (11), and with the definition of the Reynolds number, this equation leads to

$$\mathbf{C}_f = \frac{2\epsilon D_h^2 (\mathbf{K}_{int} \cdot \mathbf{R})^{-1}}{\mathrm{Re}_{D_h}} (1 + f). \tag{30}$$

3.3.1. Transverse direction

The friction coefficient in the transverse direction is calculated with Eq. (30)

$$C_{f_x} = \frac{2\epsilon D_h^2 K_{int,xx}^{-1}}{\mathrm{Re}_{D_h}} (1 + f). \tag{31}$$

According to the value of $K_{int,xx}$ given by Eq. (13), we obtain

$$C_{f_x} = \frac{310.61}{\mathrm{Re}_{D_h}} (1 + f). \tag{32}$$

Figure 9 compares the proposed wall friction coefficient C_{f_x} in laminar regime with $f = 0$ (Darcy) and f given by equation (24) (regime fit). The inertial corrections clearly impact the value of the friction coefficient as the Reynolds number increases. The same figure shows a comparison of the proposed model with literature models of the friction coefficient in the laminar regime or models using the permeability concept and with correlations in the turbulent regime usually used for CATHARE simulations. Butterworth (1979) proposed a correlation for *low flows* from experimental data performed in square arrays of tubes for different pitch-to-diameter ratio ($1.25 \leq p/d \leq 2$) and found correlated K_{xx} from p, d, and D_h. For *high flows*, Butterworth (1979) also correlated the permeability $K_{xx,\mathrm{high}}$ from experimental data using the Reynolds number defined as $Re_{df} = \rho V_f d/\mu$. For *intermediate flows*, the permeability is obtained from

$$\frac{1}{K_{xx}^2} = \frac{1}{K_{xx,\mathrm{low}}^2} + \frac{1}{K_{xx,\mathrm{high}}^2}. \tag{33}$$

In the intermediate flow regime (roughly for $50 < Re_{D_h} < 200$), the proposed model, accounting the inertial effects, tends to calculate lower friction coefficients compared to the Butterworth correlations (see Figure 9).

From a transverse friction factor model obtained in in-line tube banks, Hu (1982) derived a correlation for the permeability given by

$$K_{xx} = pD_h/[(140(d/p)^{1.6} p/(p-d)] \tag{34}$$

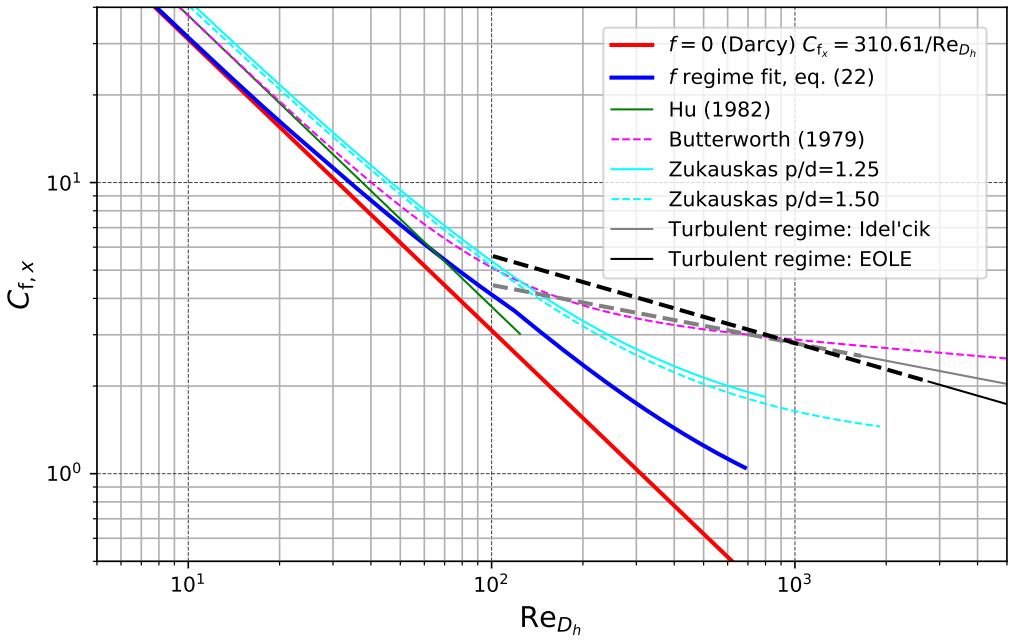

Figure 9: Comparison of the proposed friction coefficient C_{f_x} and other models in laminar and turbulent regimes for pure transverse flows.

for $1.25 \leq p/d \leq 1.5$. The intrinsic permeability obtained in the transverse direction $K_{xx} = 4.94 \times 10^{-7}$ m^2 (equation (13)) is consistent with these literature models but a little higher. As a consequence, in the Darcy regime, the proposed model for $C_{f,x}$ is slightly lower but consistent with the models of the form $C_f = A/Re$ where A can be obtained using expression (30) from the Butterworth or Hu correlations.

Literature models for the friction coefficient, like those used for comparison hereinafter, are usually expressed using the maximum velocity at the narrowest gap of the subchannel V_{gap} and the tube diameter d, the Reynolds number being calculated using these quantities, i.e. $Re_d = \rho V_{gap} d/\mu$. In order to compare the corresponding friction coefficients $C_f(Re_d)$ with the proposed model, we have converted them into $C_f(Re_{Dh})$ (see Appendix A).

In the laminar regime, Zukauskas and Ulinskas (1983) proposed empirical correlations obtained from experimental data for different p/d ratios. For $p/d = 1.25$ and $p/d = 1.50$ pitch-to-diameter ratios the correlation are of the

form

$$Eu = \sum_{i=0}^{n} A_i / Re_d^i \tag{35}$$

where Eu is the Euler number, defined by $Eu \equiv \Delta P/(1/2\rho V_{gap}^2)$ where ΔP is the pressure drop across a single row of the tube bank. Compared to the proposed model with the Forchheimer correction $C_f = A/Re(1+f)$, where f has a polynomial expression $f = \sum_i a_i Re^i$, equation (35), with $n = 3$ for $p/d = 1.25$ and $n = 2$ for $p/d = 1.50$, resulting from a fit to the experimental data, may be also considered as taking into account the inertial effects (and/or the transition to the turbulent regime) when the Reynolds number increases. Indeed, the proposed model with the inertial correction f has the same behavior as the Zukauskas correlations. The friction coefficient calculated with the proposed model for $p/d = 1.326$ corresponding the studied PWR subchannel is nevertheless lower compared to those obtained by Zukauskas correlations obtained for $p/d = 1.25$ and $p/d = 1.50$ pitch-to-diameter ratios. The proposed friction coefficient shows a *significant difference* of the calculated friction coefficient using EOLE or Idel'cik correlations established in the turbulent regime if these models are extrapolated to the transition and laminar regimes.

3.3.2. Axial direction

Similar calculations were performed for axial flows. The wall friction coefficient is deduced from Eq. (30) and the value of the intrinsic permeability in Eq. (13):

$$C_{f_z} = \frac{2\epsilon D_h^2 K_{int,zz}^{-1}}{\mathrm{Re}_{D_h}}(1+f). \tag{36}$$

No inertial effect is expected in this situation, thus the expression for C_{f_z} is

$$C_{f_z} = \frac{99.9}{\mathrm{Re}_{D_h}}. \tag{37}$$

In Cheng and Todreas (1986), a correlation of the friction factor based on experimental results in square arrays of tubes was proposed for laminar flow

$$C_{f_z} = \frac{A_z}{Re_{D_h}}, \tag{38}$$

in which A_z is a constant depending on the pitch-to-diameter ratio p/d of the array. The value of A_z for a typical PWR type rod bundle ($p/d = 1.326$)

is 101.35 according to Cheng and Todreas (1986). A similar result was also found by a relation established from numerical simulations by Moorthi and Sharma (2018), where the value of A_z for a PWR type rod bundle is 100.44 for a laminar flow, see Table 1. In this paper, the value of A_z calculated for a PWR type rod bundle is 99.9. Considering that in both studies mentioned above the results are calculated with a relation based on the ratio of pitch to diameter, this discrepancy is in a reasonable range compared to uncertainty, which is about 10% in Cheng and Todreas (1986).

Table 1: Comparison of models for A_z in laminar regime.

Reference	Correlation for A_z	Value for $p/d = 1.326$
(Cheng and Todreas, 1986)	$A_z = a + b_1(p/d-1) + b_2(p/d-1)^2$ $a = 35.55, b_1 = 263.7, b_2 = -190.2$	101.4
(Moorthi and Sharma, 2018)	$A_z = (59.34p/d - 55.13)/(p/d - 0.3881)$	100.4
Current study		99.9

4. Test case: impact of apparent permeability models in a rod bundle with non-uniform inlet velocities

In this section, we study the relative effects of constitutive models on the mixing process along a rod bundle in a case of non-uniform inlet flow. Computations are performed with a dynamic viscosity of 10^{-3} Pa·s, a density of $\rho = 10^3$ kg/m^3. The domain is represented in Figure 10. It consists of 2 parallel rows of 2×17 PWR rods. Symmetry conditions are imposed on lateral boundary conditions. The pressure is uniform at outlet. For the inlet velocities, we imposed a left/right asymmetry with the inlet axial velocity equal to $V_{\text{in,left}}$ on the left and equal to $V_{\text{in,right}}$ on the right. Three test cases with different couples $(V_{\text{in,left}}, V_{\text{in,right}})$ are considered to investigate the different regimes (weak inertia at low Reynolds number, transition, and strong inertia at higher Reynolds number), see Table 2.

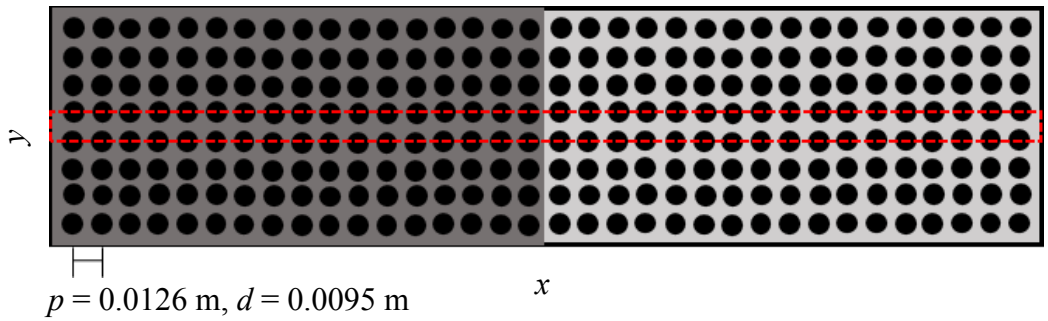

Figure 10: Cross section of a rod bundle including 8×34 unheated rods representing 2 half assemblies. The computation domain is the central row of subchannels circled by red dashed line with height H =1.26 m.

This may be summarized as

$$\mathbf{n} \cdot \mathbf{V}_f = 0, \quad \text{at } x = 0 \text{ m and } x = 0.4284 \text{ m} \tag{39a}$$

$$\mathbf{n} \cdot \mathbf{V}_f = V_{\text{in,left}}, \quad \text{at } z = 0 \text{ m and } x \leq 0.2142 \text{ m} \tag{39b}$$

$$\mathbf{n} \cdot \mathbf{V}_f = V_{\text{in,right}}, \quad \text{at } z = 0 \text{ m and } x > 0.2142 \text{ m} \tag{39c}$$

$$P = P_{out} = 10^5 \text{Pa}, \quad \text{at } z = 1.26 \text{ m} \tag{39d}$$

Table 2: Considered test cases with different inlet velocities and the corresponding Reynolds numbers.

Test case	$V_{\text{in,left}}$ (m/s)	$V_{\text{in,right}}$ (m/s)	$Re_{Dh,\text{left}}$	$Re_{Dh,\text{right}}$
1	0.05	0.01	590	118
2	0.05	0.005	590	59
3	0.05	0.001	590	12

Because of pressure differences in the transverse direction, a transverse flow is generated that progressively equalizes along the axial direction. In order to capture the full equalization process, the computation is run along a sufficient height (H =1.26 m) and we study how it evolves to assess the accuracy of the 3D rod friction model. We compare three classes of results

1. the finite-element implementation of the generalized Darcy-Forchheimer approach in FEniCS

2. CATHARE 3 without modifying the friction coefficients, which we will refer to as standard CATHARE
3. CATHARE 3 with integration of our constitutive relations for the friction coefficients.

4.1. Impact of f and $\mathbf{R}$ on the relaxation of the left/right velocities

For test case 1 defined in Table 2, we start by comparing the two cases $f = 0$, $\mathbf{R} = \mathbf{I}$ (linear Darcy) and f given by equation (25), $\mathbf{R} = \mathbf{R_y}(\gamma_\mathbf{y})$ in FEniCS.

Figure 11 shows the axial and transverse velocity variation along the x-axis at different elevations. The asymmetry in inlet velocities is balanced by the transverse flow, which is mainly significant in the central zone, and the equalization occurs at $z \sim 0.8$ m. The maximal transverse velocity normalized by the largest inlet velocity (on the left) is ~ 0.8, which is of the same order as the axial velocity. This peak is obtained close to the inlet, as a result of the discontinuity of velocities in the middle of the boundary condition. Transverse velocities get smaller in the transverse direction as we get away form the discontinuity. Transverse velocities also decrease in the axial direction as we get away from the inlet condition. We further observe that the transverse velocity with inertia is smaller than without, so that the axial velocity takes longer to equalize, in particular near boundary regions on the left. In addition, the transverse velocity is symmetrical about the median interface for the linear Darcy's law but asymmetric for the inertial case. This is because non-linear effects are stronger on the side with the higher velocity.

The rotation matrix tends to rotate the velocity towards the transverse direction in this situation, as shown in Figure 2b. However, since the rotation angle is usually small, with a maximal value of γ_y of about $4°$, we expect the decrease caused by f to play a dominant role. To gain further insight into the relative impact of f and $\mathbf{R}$, we have imposed $f = f(Re_{Dh}, \alpha)$ (eq. (25)) and study the two cases $\mathbf{R} = \mathbf{I}$ or $\mathbf{R} = \mathbf{R}(\gamma_y)$ for the rotation matrix. The transverse and axial velocity profiles are presented in Figure 11, showing almost no effect of the rotation matrix. Results show that f can decrease the transverse velocity and slightly delay the balancing process.

4.2. Comparison with CATHARE

In CATHARE, the numerical method is based on finite volume discretization with staggered structured mesh. The donor cell principle is used for the

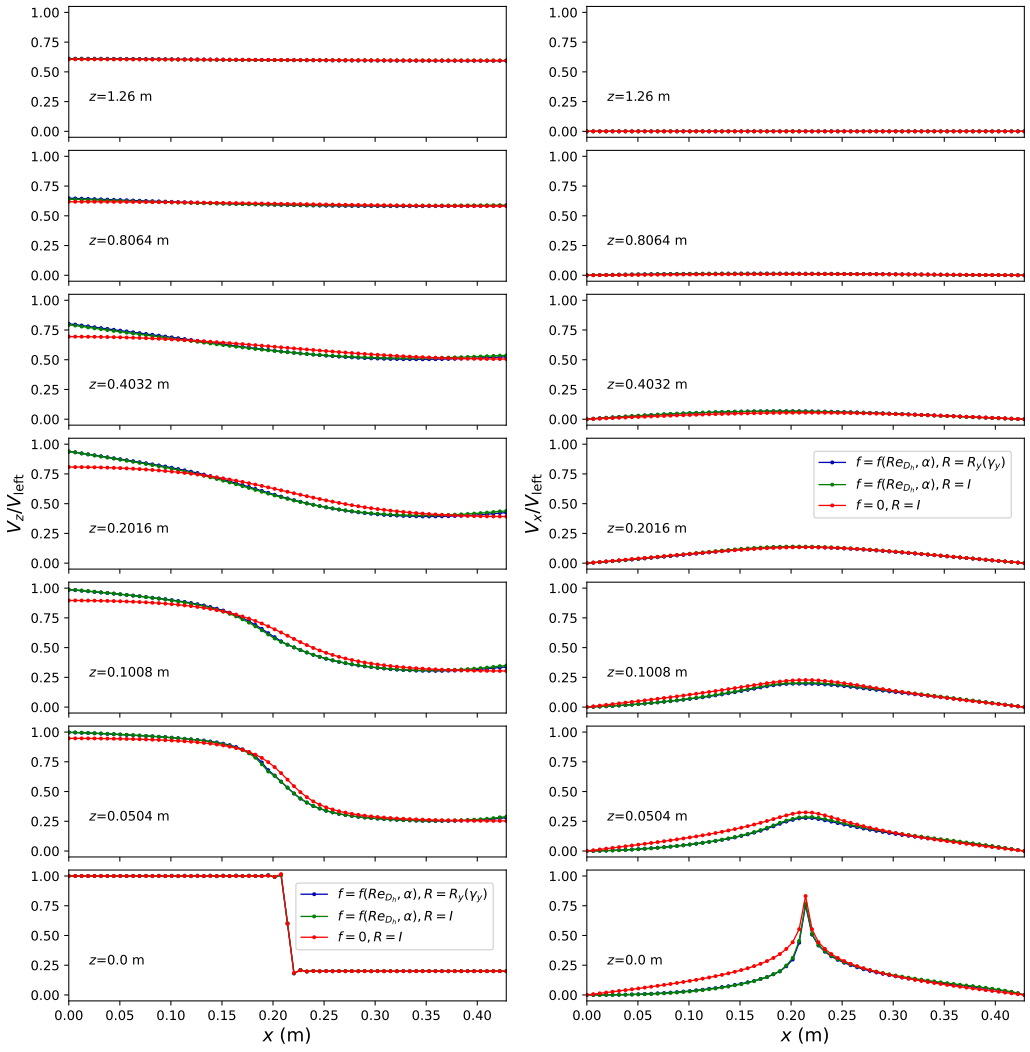

(a) (b)

Figure 11: Test case 1 – FEniCS results calculated with $f = f(Re_{Dh}, \alpha)$ (eq. (25)), $\mathbf{R} = \mathbf{R}_y(\gamma_y)$, with $f = f(Re_{Dh}, \alpha)$, $\mathbf{R} = \mathbf{I}$, and $f = 0$, $\mathbf{R} = \mathbf{I}$. Comparison of (a) axial velocities normalized by left inlet velocity and (b) transverse velocities normalized by left inlet velocity.

convective terms. The time discretization for these 3D equations is based on a semi-implicit scheme (Dor et al., 2013).

For the considered tests, a 3D cartesian mesh has been chosen so that the cells coincide with the subchannels (one mesh per subchannel in the (x, y)-plane). In the z direction, the computational domain (1.26 m) is divided in 100 uniform cells, so each cell has a height equal to 1.26 cm. The total number of mesh elements is thus $34 \times 100 = 3400$. Due to the numerical method, the velocities are calculated on the faces in the mesh. As a consequence, the inlet velocity on the central face is set as the average of the left and right velocities, $V_{\text{in,center}} = \frac{1}{2}(V_{\text{in,left}} + V_{\text{in,right}})$.

CATHARE 3 calculations have been carried out using the standard version of the code (referred to as "Standard") and using our constitutive relations (32)(37) for the friction coefficients (referred to as "New"), taking $\mathbf{R} = \mathbf{I}$ (the tensor $\mathbf{C}_f$ is diagonal in equation (30)) with the Darcy model ($f = 0$ in equation (32)) and the Darcy-Forchheimer model. For test case 1, Figure 12a shows the normalized axial velocity ($V_z/V_{\text{in,left}}$) profile along the x-axis at different elevations for the 3 simulations. Results obtained using the new CATHARE 3 Darcy model are similar to those obtained with the standard model, and the velocity equilibrium between the left and right parts of the domain tends to occur slightly earlier. Consistent with results obtained using FEniCS, the Darcy-Forchheimer model has a significant impact on the velocity profiles. Comparison between CATHARE 3 and FEniCS simulations using the Darcy-Forchheimer model with $\mathbf{R} = \mathbf{I}$ is given in Figure 12b. Results are overall in a good agreement, allowing us to verify the transposition of the porous approach with an apparent permeability to the friction tensor model in CATHARE. Some differences exist near the inlet of the simulation domain that are due to the treatment of the inlet velocities. At the inlet ($z = 0$ m), transverse velocities are set to 0 in the case of CATHARE 3 and not in the FEniCS approach. Moreover, as already mentioned, the inlet velocity in the central face at the inlet boundary in the CATHARE 3 simulations is the average of the velocities imposed in the left and right parts of the domain. The same conclusions can be drawn for the test cases 2 and 3, where the velocity on the right-hand side of the inlet is reduced (Figures 13a and 13b). For case 3, Figure 14 shows the velocity field calculated by CATHARE 3 using the Darcy-Forchheimer model with $\mathbf{R} = \mathbf{I}$. At the center of the domain, close to the entrance, the angle α of the velocity vectors with respect to the z-direction are higher than 45°, and thus the angle factor $\Phi(\alpha) = 1$, implying that the friction coefficient only depends on the Reynolds number according to the proposed model (25).

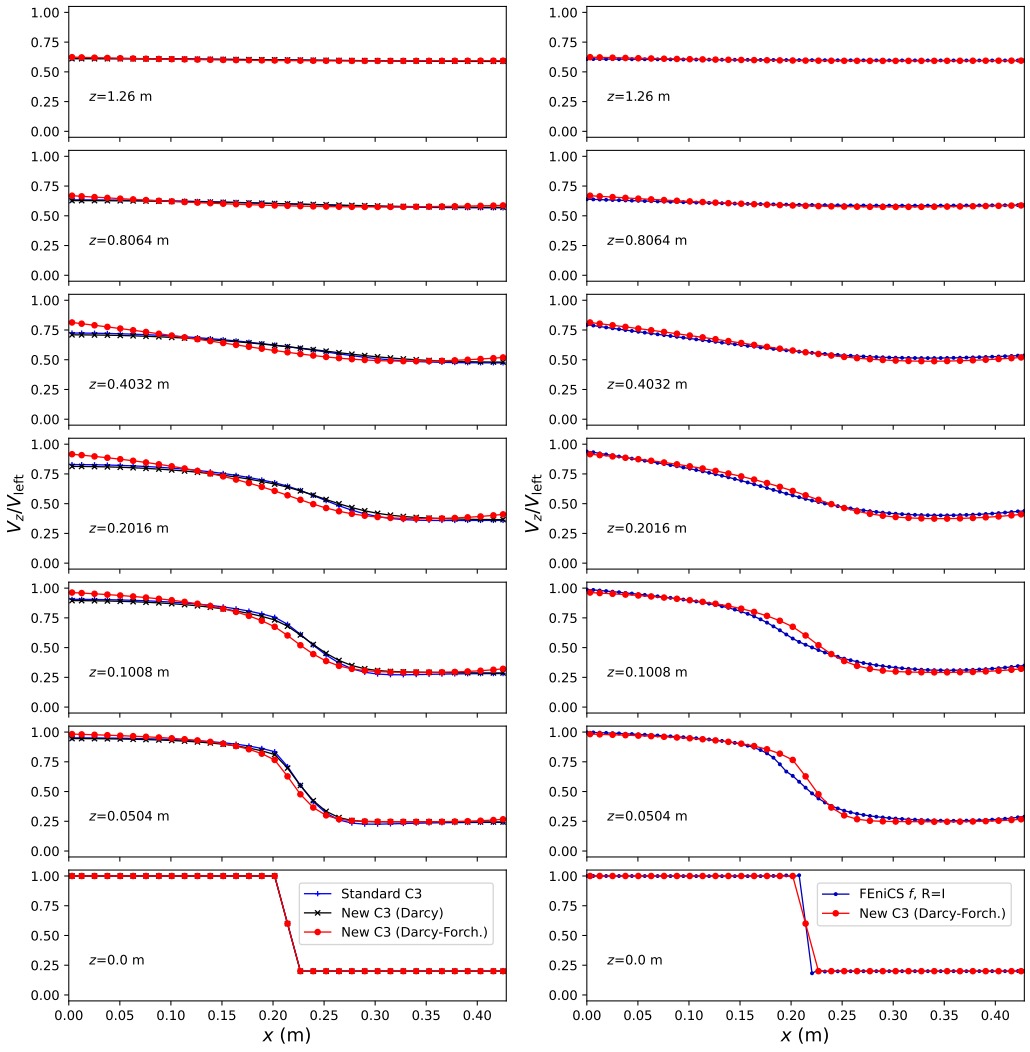

(a) (b)

Figure 12: Test case 1 – Calculation results with CATHARE 3 and with FEniCS (normalized axial velocity $V_z/V_{\text{in,left}}$ profiles along the x-axis at different elevations). (a) Comparison of simulations using the standard CATHARE 3 model, the implemented Darcy model ($f = 0$) and the Darcy-Forchheimer model with $\mathbf{R} = \mathbf{I}$ in CATHARE 3. (b) Comparison of simulation between CATHARE 3 and FEnicS for the Darcy-Forchheimer model with $\mathbf{R} = \mathbf{I}$.

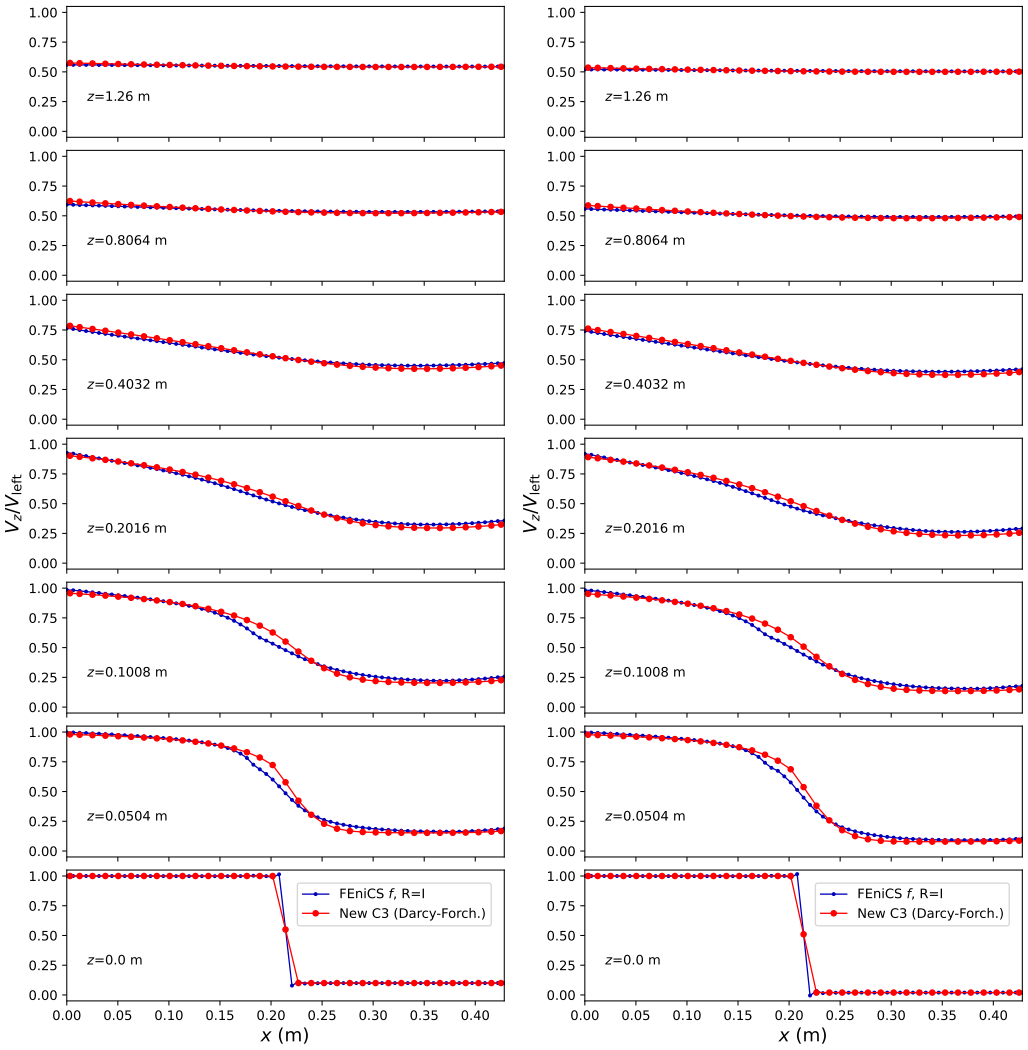

(a) Case 2 (b) Case 3

Figure 13: Test cases 2 and 3 – Calculation results with CATHARE 3 and FEniCS (normalized axial velocity $V_z/V_{\text{in,left}}$ profiles along the x-axis at different elevations).

5. Discussion about possible extensions

In this section, we discuss the possible extension of the proposed approach to two problems of practical interest in the engineering context of nuclear

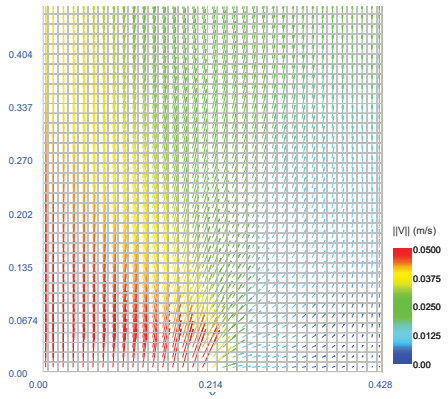

Figure 14: Case 3 – Velocity field calculated by CATHARE 3 at the bottom of the simulation domain using the Darcy-Forchheimer model with $\mathbf{R} = \mathbf{I}$. Velocity vectors are colored in accordance to their magnitude.

reactors:

1. single-phase flow and different unit-cell geometry,
2. two-phase flow.

5.1. Different bundle geometry

The calculations made in this paper are for a bare bundle geometry. In particular, Mixing Vane spacer Grids (MVG) are not taken into account. In general, a different unit cell, unless obtained by a geometrical similitude, would require to reproduce the entire sequence of pore-scale unit-cell calculations and correlation identification, before using the obtained effective properties in macro-scale simulations. A different organization of the bare rod bundle would not pose additional difficulties. On the contrary, taking into account the existence of MVGs would impose important adaptations. In the laminar regime, effect of this type of grid on the flow was studied in the Rod Bundle Heat Transfer (RBHT) test section (Mohanta et al., 2017), including 7×7 electrically heated rods with the same diameter and pitch as those considered in this paper, where the redevelopment length is indicated at $z/D_h > 25$ for $Re = 500$, that is around the half of the distance between two spacer grids. Durbin et al. (2010) obtained measurements of the velocity at $Re = 100$ and $Re = 900$ in a prototypical PWR rod bundle and showed the influence of the grid far downstream depends its type, with an effect due to the wake extending to the mid-distance of two spacers grids at

$Re = 900$ for split type mixing vanes. According to this study, the idealized laminar approach is valid at low Reynolds number ($Re = 100$), but deviated from this approach at $Re = 900$ due the cross flows, secondary flows, and velocity fluctuations induced by the MVG. Concerning the extension of the model to MVG consideration in the Reynolds number range ($Re < 600$) of our study, a straightforward approach, while certainly highly demanding in terms of computations, would consider a new 3D unit cell involving a portion of the rod bundle, or likely the entire assembly, and the MVG structure. Another option is to add a macro-scale singularity, or to build a Darcy-scale heterogeneous effective medium, with some regions including the effect of MVGs. Whatever the adopted strategy, as usual in multi-scale analysis, one should verify that the assumption of scale separation is still valid, otherwise the macro-scale model would be inaccurate. Indeed, several problems can be contemplated:

- Macro-scale flow pattern may show characteristic length-scales, e.g. convective vortices, on the same order as the unit cell characteristic length. Since the size of new 3D unit cell is larger than the one for a bare bundle, this is likely to affect more drastically the accuracy of macro-scale modeling in the case of bundle with MVG.

- The question of *effective boundary conditions* has not been examined thoroughly in this paper. Questions arise when the length-scale characterizing pressure and velocity distributions at the boundaries are much smaller than the unit-cell characteristic length. Again, it is likely to have a greater impact in the case of a bundle with MVG, given the impact of the structure over a larger area.

It should be emphasized that these limitations are not specific to the macro-scale model proposed herein.

5.2. Two-Phase flow

The question of developing a macro-scale model for the case of two-phase flow is more difficult. It is beyond the scope of this paper to give a thorough presentation of the theoretical problems at stake, and we refer the reader to Davit and Quintard (2019) for a more extensive review. It is fair to say that a rigorous development, based on upscaling techniques, of two-phase flow macro-scale models remains largely an open problem. The heuristic Muskat model (Muskat (1949)) has been extended to inertia flow by adding

a quadratic term (Ergun (1952)) weighted by a function of saturation. A heuristic method, the two-phase frictional multiplier approach (more details are given in the Conclusion), also used in classical nuclear engineering code. Of course, this approach, could also be used in the case of this paper proposed model. At least, it would offer the possibility to take into account the various inertia regimes, on one hand, and also anisotropic effects induced by the non-linear features. Such an approach raises several questions, as discussed below. Two-phase flow phenomenology is rather complex, and it is likely a crude approximation to assume that pressure drop can be split into two independent terms, one coming from the analysis of one-phase flow in the given structure, the other from the phase partition. Lack of regimes and anisotropy effects is not the only shortcut of the Ergun-like approaches. The mathematical structure of the momentum balance equations is also questionable. Indeed, upscaling techniques in the case of a quasi-steady interface leads to a form of generalized Darcy's law with additional cross-terms (Whitaker (1986); Lasseux et al. (1996)). These cross-terms are often discarded in applications involving low permeability porous media, but they play a very important role in highly permeable media, as illustrated in Taherzadeh and Saidi (2015); Clavier et al. (2017) in the context of nuclear safety. Multi-scale analysis of two-phase flow in porous media has also led to more complex dynamic models, as illustrated for instance in Kalaydjian (1987), Quintard and Whitaker (1990), Hassanizadeh and Gray (1993), Hilfer (1998), Cueto-Felgueroso and Juanes (2009). These modeling proposals may be analysed and adapted in nuclear engineering. To summarize this discussion, Ergun type of approach is feasible with the proposed model, it would consist into adding inertia terms coming from the one-phase flow analysis weighted by a function of saturation (often called passability). Of course, the above discussion indicates that this approach is not fully supported by theoretical and experimental evidence, under all flow conditions. A warning that deserves further investigation.

6. Conclusion

Modeling flows in a PWR core in accidental scenarios characterized by relatively low Reynolds numbers and potentially high transverse flows requires an adaptation of the macro-scale models used in classical codes, such as the code CATHARE used in this paper.

The modifications proposed in this work are based on our analysis of the

upscaling of laminar flows in porous media. The intrinsic permeability is modified by the application of a rotation operator, $\mathbf{R}$, and a non-linear scaling, f, both depending on the average velocity magnitude and orientation. These modifications have been determined quantitatively for a typical rod bundle geometry. The workflow relies upon: (i) direct numerical simulations in a representative unit cell of a rod bundle for various values of the velocity magnitude and orientations, (ii) the development of simple correlations representing the numerical results.

The resulting f and $\mathbf{R}$ were subsequently used to propose adaptation of the CATHARE code constitutive models in the case of low Reynolds number regimes ($Re_{Dh} < 600$). The original correlations as well as the modified CATHARE constitutive models were tested in the modeling of a flow case with a non uniform entrance velocity generating transverse flows. We observed that f had a major impact on the results, while $\mathbf{R}$ did not contribute significantly (less than 5° additional rotation). This latter remark suggests that the modified CATHARE constitutive models may be useful, even though they lack the additional orientation effects due to inertia.

A direct perspective of this work would be to complete the construction of the constitutive models for all velocity orientations. It would also be interesting to test the proposed model in different cases, in particular with the objective of having more pronounced transverse flows, like, for instance, in the case of a natural convection vortex.

Regarding the applicability of the proposed method, it may be easily extended to other PWR cores or other square lattice cores where the pitch p and the rod diameter d are different as those considered. In the case, the proposed model have to adapted to the new geometry by performing new CFD simulations, allowing to determine at least other coefficients for the axial term of the friction model. The same conclusion is drawn for transverse flows or inclined flows. If a sufficient number of different pitches and diameters is considered, the model could be generalized, as (Moorthi and Sharma, 2018) proposed in the case of axial flow, considering p/d as the parameter of the model. Account of the effect of the mixing vane grids on the friction model is more difficult, as discussed in Sec. 5.

The model can also be applied to estimate the friction in pure steam flow above the core water swell level, at low Reynolds number. It has to be supplemented or to be extended by other models in the transition zone between the laminar and turbulent regimes, and in the full turbulent regime. Regarding the case of two-phase flow, in particular during the reflooding

phase of a LBLOCA or the uncovery phase of a SBLOCA or IBLOCA, the model may be extended as discussed more thoroughly in Sec. 5, or may be set as the based single-phase friction model, if a classical approach is used by introducing a two-phase multiplier factor, to determine the two-phase pressure drop, see e.g. (Dowlati et al., 1990) or (Herer, 2023). This approach is adopted in the 6-equation model in the CATHARE code, where the axial friction coefficient for each phase is deduced from the single-phase coefficient using a two-phase Reynolds number and the two-phase multipliers factors are function of the void fraction, among other parameters relative to the flow conditions (Bestion, 1990). Nevertheless, if this approach is classic in the case of co-current gas-liquid flows, the difficulty is to extend it to 3D flows, where the liquid and the gas velocity vectors may have different directions. While several proposals have been made in the recent decades to model multiphase flow in highly permeable media, i.e., cases with small capillary effects but potentially large inertia effects (see review in Davit and Quintard (2019)), this problem remains largely open in terms of the appropriate mathematical structure of the transport equations, as well as in terms of effective properties and their dependence on the velocities orientations and saturation. Therefore, additional work is needed to assess the applicability of the models to generic two-phase flow situations of interest in the context of nuclear engineering.

Appendix A. Calculation of $C_{f,x}$ from literature models

In a pure transverse crossflow, literature models usually expressed the pressure loss coefficient K_T (K_T is the Euler number in Zukauskas correlation) as

$$\Delta P = \frac{1}{2} K_T \rho V_{gap}^2 \tag{A.1}$$

K_T is also usually correlated to the Reynolds number $Re_d = \rho V_{gap} d/\mu$ based on the gap velocity V_{gap} and the tube diameter d, i.e. $K_T = K_T(Re_d)$. In our approach, the pressure gradient due to the wall friction accross a single row in the transverse direction x is given by (see equations (19) and (21))

$$\frac{\Delta P}{\Delta x} = -\tau_{w,x} = \frac{1}{2D_h} \rho C_{f,x} V_x |V_x| \tag{A.2}$$

In the previous expression, $\Delta x = p$ if a single row is considered. Velocities V_{gap} and V_x can be deduced from each other using the expression

$$V_{gap} = \frac{p/d}{p/d - 1}\epsilon V_x \tag{A.3}$$

and thus the relation between Re_{Dh} and Re_d is

$$Re_d = Re_{Dh}\frac{d}{D_h}\frac{p/d}{(p/d) - 1}\epsilon \tag{A.4}$$

From equations (A.1)–(A.4), the coefficient $C_{f,x}$ depending on the Reynolds number Re_{Dh} can be deduced:

$$C_{f,x}(Re_{Dh}) = \frac{D_h}{p}\left(\frac{\epsilon(p/d)}{(p/d) - 1}\right)^2 K_T(Re_d(Re_{Dh})) \tag{A.5}$$

References

Agnaou, M., Lasseux, D., Ahmadi, A., 2016. From steady to unsteady laminar flow in model porous structures: an investigation of the first Hopf bifurcation. Computers & Fluids 136, 67–82. doi:10.1016/j.compfluid.2016.05.030.

Alku, T., 2017. Modelling of turbulent effects in LOCA conditions with CATHARE-3. Nuclear Engineering and Design 321, 258–265. doi:10.1016/j.nucengdes.2016.10.050.

Alnæs, M., Blechta, J., Hake, J., Johansson, A., Kehlet, B., Logg, A., Richardson, C., Ring, J., Rognes, M.E., Wells, G.N., 2015. The FEniCS project version 1.5. Archive of Numerical Software 3. doi:10.11588/ans.2015.100.20553.

Angeli, P.E., Bieder, U., Fauchet, G., 2015. Overview of the TrioCFD code: Main features, V&V procedures and typical applications to nuclear engineering, in: Proceedings of the 16th International Topical Meeting on Nuclear Reactor Thermalhydraulics (NURETH-16), Chicago, USA.

Bestion, D., 1990. The physical closure laws in the CATHARE code. Nuclear Engineering and Design 124, 229–245. doi:10.1016/0029-5493(90)90294-8.

Bestion, D., Fillion, P., 2019. Revisiting the PIRT and scaling analysis within the frame of 3D system code modelling, in: NURETH-18, Portland, OR, USA.

Bestion, D., Fillion, P., Gaillard, P., Valette, M., 2017. 3D core thermohydraulic phenomena in PWR SBLOCAs and IBLOCAs, in: NURETH-17, Xi'an, China. URL: https://hal.science/hal-02433889.

Bestion, D., Fillion, P., Préa, R., Bernard-Michel, G., 2018. Improved PWR LOCA Simulations Through Refined Core 3D Simulations – An Advanced 3D Modelling and the Associated METERO Validation Program, in: NUTHOS-12, Qingdao, China. URL: https://cea.hal.science/cea-04084545.

Bieder, U., Falk, F., Fauchet, G., 2014. LES analysis of the flow in a simplified PWR assembly with mixing grid. Progress in Nuclear Energy 75, 15–24. doi:10.1016/j.pnucene.2014.03.014.

Bieder, U., Ziskind, G., Rashkovan, A., 2018. CFD analysis and experimental validation of steady state mixed convection sodium flow. Nuclear Engineering and Design 326, 333–343. doi:10.1016/j.nucengdes.2017.11.028.

Butterworth, D., 1979. The correlation of cross-flow pressure drop data by means of the permeability concept. AERE-R 9435, UKAEA Atomic Energy Research Establishment.

Chandesris, M., Mazoyer, M., Serre, G., Valette, M., 2013. Rod bundle thermalhydraulics mixing phenomena: 3D analysis with CATHARE 3 of various experiments, in: Proceedings of the 15th International Topical Meeting on Nuclear Reactor Thermal-hydraulics (NURETH-15), Pisa, Italy.

Cheng, S.K., Todreas, N.E., 1986. Hydrodynamic models and correlations for bare and wire-wrapped hexagonal rod bundles—bundle friction factors, subchannel friction factors and mixing parameters. Nuclear Engineering and Design 92, 227–251. doi:10.1016/0029-5493(86)90249-9.

Clavier, R., Chikhi, N., Fichot, F., Quintard, M., 2017. Modeling of Inertial Multi-Phase Flows through High Permeability Porous Media: Friction Closure Laws. International Journal of Multiphase Flow 91, 243–261. doi:10.1016/j.ijmultiphaseflow.2017.02.003.

Cueto-Felgueroso, L., Juanes, R., 2009. A phase field model of unsaturated flow. Water Resources Research 45, 1–23. doi:10.1029/2009WR007945.

Cumo, M., Farello, G., Gasiorowski, J., Iovino, G., Naviglio, A., 1980. Quality influence on the departure from nucleate boiling in cross flows through bundles. Nuclear Technology 49, 337–346. doi:10.13182/NT80-A17682.

Davit, Y., Quintard, M., 2019. One-phase and two-phase flow in highly permeable porous media. Heat Transfer Engineering 40, 391–409. doi:10.1080/01457632.2018.1432018.

De Lemos, M.J., 2012. Turbulence in porous media: modeling and applications. Elsevier.

Dor, I., Chandesris, M., Germain, P., Ruby, A., 2013. CATHARE 3D module from CATHARE 2 V2.5_3 to CATHARE 3 V1.0, in: NURETH-15, Pisa, Italy.

Dowlati, R., Kawaji, M., Chan, A.M.C., 1990. Pitch-to-diameter effect on two-phase flow across an in-line tube bundle. AIChE Journal 36, 765–772. doi:10.1002/aic.690360513.

Durbin, S., Lindgren, E., Zigh, A., 2010. Measurement of laminar velocity profiles in a prototypic PWR fuel assembly, in: Computational Fluid Dynamics (CFD) for Nuclear Reactor Safety Applications CFD4NRS-3, Bethesda, Maryland, USA. URL: https://oecd-nea.org/nsd/csni/cfd/workshops/CFD4NRS-3/poster-papers/session-2/P2-5.pdf.

Ebeling-Koning, D.B., Robinson, J.T., Todreas, N.E., 1986. Models for the fluid-solid interaction force for multidimensional single phase flow within tube bundles. Nuclear engineering and design 91, 29–40. doi:10.1016/0029-5493(86)90182-2.

Ergun, S., 1952. Fluid flow through packed columns. Chem. Eng. Prog. 48, 89–94.

Forchheimer, P., 1901. Wasserbewegung durch Boden. Z. Ver. Deutsch, Ing. 45, 1782–1788.

Fu, Q., Bestion, D., Fillion, P., Davit, Y., Quintard, M., 2019. Analysis of flow in rod bundles with velocity and temperature radial dissymmetry using CATHARE-3, in: ICAPP 2019 – International Congress on Advances in Nuclear Power Plants, Juan-les-pins, France. URL: https://hal.science/hal-02380403.

Hassanizadeh, M., Gray, W.G., 1993. Toward an improved description of the physics of two-phase flow. Advances in Water Resources 16, 53–67. doi:10.1016/0309-1708(93)90029-F.

Herer, C., 2023. CSNI status report "3D capabilities of thermalhydraulic system codes": Lessons learned. Nuclear Engineering and Design 405, 112188. doi:10.1016/j.nucengdes.2023.112188.

Hilfer, R., 1998. Macroscopic equations of motion for two-phase flow in porous media. Physical Review E 58, 2090–2096. doi:10.1103/PhysRevE.58.2090.

Hosseini, S.H., Shojaee, S., Ahmadi, G., Zivdar, M., 2012. Computational fluid dynamics studies of dry and wet pressure drops in structured packings. Journal of Industrial and Engineering Chemistry 18, 1465–1473. doi:10.1016/j.jiec.2012.02.012.

Hu, M., 1982. Anisotropic modelling of tube bundle flow during steam generator wet layup. Nuclear Engineering and Design 71, 151–160. doi:10.1016/0029-5493(82)90126-1.

Idel'Cik, I.E., 1969. Mémento des pertes de charge. Collection de la Direction des Etudes et Recherches d'Electricite de France, Eyrolles, Paris.

Jin, Y., Uth, M.F., Kuznetsov, A.V., Herwig, H., 2015. Numerical investigation of the possibility of macroscopic turbulence in porous media: a direct numerical simulation study. Journal of Fluid Mechanics 766, 76. doi:10.1017/jfm.2015.9.

Kalaydjian, F., 1987. A macroscopic description of multiphase flow in porous media involving spacetime evolution of fluid/fluid interface. Transport in Porous Media 2, 537–552. doi:10.1007/BF00192154.

Lasseux, D., Abbasian Arani, A.A., Ahmadi, A., 2011. On the stationary macroscopic inertial effects for one phase flow in ordered and disordered porous media. Physics of fluids 23, 073103. doi:10.1063/1.3615514.

Lasseux, D., Quintard, M., Whitaker, S., 1996. Determination of Permeability Tensors for Two-Phase Flow in Homogeneous Porous Media: Theory. Transport in Porous Media 24, 107–137. doi:10.1007/BF00139841.

Mohanta, L., Cheung, F.B., Bajorek, S.M., Tien, K., Hoxie, C.L., 2017. Experimental study of laminar mixed convection in a rod bundle with mixing vane spacer grids. Nuclear Engineering and Design 312, 99–105. doi:10.1016/j.nucengdes.2016.07.023.

Moorthi, A., Sharma, A.K., 2018. Laminar fluid flow and heat transfer in non-circular sub-channel geometries of nuclear fuel bundle. Progress in Nuclear Energy 103, 243–253. doi:10.1016/j.pnucene.2017.10.009.

Muskat, M., 1949. Physical Principles of Oil Production. McGraw-Hill, New York.

Pasquier, S., Quintard, M., Davit, Y., 2017. Modeling flow in porous media with rough surfaces: Effective slip boundary conditions and application to structured packings. Chemical Engineering Science 165, 131–146. doi:10.1016/j.ces.2017.01.063.

Pauthenet, M., Davit, Y., Quintard, M., Bottaro, A., 2018. Inertial sensitivity of porous microstructures. Transport in Porous Media 125, 211–238. doi:10.1007/s11242-018-1115-1.

Peybernes, J., 2005. Evaluation of the forces generated by cross-flow on PWR fuel assembly. IAEA-TECDO 1454, 13.

Préa, R., Fillion, P., Matteo, L., Mauger, G., Mekkas, A., 2020. CATHARE-3 V2.1: the new industrial version of the CATHARE code, in: Advances in Thermal Hydraulics (ATH '20). URL: https://cea.hal.science/cea-04087378.

Quintard, M., Whitaker, S., 1990. Two-phase flow in heterogeneous porous media I: The influence of large spatial and temporal gradients. Transport in Porous Media 5, 341–379. doi:10.1007/BF01141991.

Rehme, K., 1973. Pressure drop correlations for fuel element spacers. Nuclear technology 17, 15–23. doi:10.13182/NT73-A31250.

Rojas, S., Koplik, J., 1998. Nonlinear flow in porous media. Physical Review E 58, 4776. doi:10.1103/PhysRevE.58.4776.

SALOME, 2023. URL: https://www.salome-platform.org/.

Skjetne, E., Auriault, J., 1999. New insights on steady, non-linear flow in porous media. European Journal of Mechanics-B/Fluids 18, 131–145. doi:10.1016/S0997-7546(99)80010-7.

Soulaine, C., Quintard, M., 2014. On the use of a Darcy–Forchheimer like model for a macro-scale description of turbulence in porous media and its application to structured packings. International Journal of Heat and Mass Transfer 74, 88–100. doi:10.1016/j.ijheatmasstransfer.2014.02.069.

Sung, Y., Kucukboyaci, V.N., Cao, L., Salko, R.K., 2015. COBRA-TF evaluation and application for PWR steamline break DNB analysis, in: NURETH-16, Chicago, IL, USA.

Taherzadeh, M., Saidi, M., 2015. Modeling of two-phase flow in porous media with heat generation. International Journal of Multiphase Flow 69, 115–127. doi:10.1016/j.ijmultiphaseflow.2014.10.013.

Valette, M., 2012. Analysis of subchannel and rod bundle PSBT experiments with CATHARE 3. Science and Technology of Nuclear Installations 2012, 123426. doi:10.1155/2012/123426.

Whitaker, S., 1986. Flow in porous media II: The governing equations for immiscible, two-phase flow. Transport in Porous Media 1, 105–125. doi:10.1007/bf00714688.

Zukauskas, A., Ulinskas, R., 1983. Heat Exchanger Design Handbook. Hemisphere Publishing Corporation. chapter Banks of plain and finned tubes. p. 2080.